

THESIS

PROBING BURIED DEFECTS IN ZINC OXIDE NANOPARTICLES USING DEFECT-
MEDIATED ENERGY TRANSFER

Submitted by

Lacey Beck

Department of Chemistry

In partial fulfillment of the requirements

For the Degree of Master of Science

Colorado State University

Fort Collins, Colorado

Summer 2019

Master's Committee:

Advisor: Justin Sambur

Amy Prieto

Randy Bartels

Copyright by Lacey Marie Beck 2019

All Rights Reserved

ABSTRACT

PROBING BURIED DEFECTS IN ZINC OXIDE NANOPARTICLES USING DEFECT-MEDIATED ENERGY TRANSFER

Semiconductor nanocrystals are actively explored as light harvesting materials for solar energy conversion and optoelectronic applications such as solar cells and light emitting diodes. The underlying processes in such systems include charge carrier generation, recombination, and transport. Defects influence these underlying processes by introducing energy levels inside the semiconductor bandgap that trap charge carriers. Despite their critical importance, the real space distribution of defect sites in semiconductor nanocrystals is often unknown. Here we demonstrate an ensemble-level energy transfer measurement approach to study the radiative defect states in a size series of ZnO nanocrystals. In this approach, ZnO defects that have energy levels inside the band gap engage in energy transfer with surface adsorbed AlexaFluor dye molecule acceptors. By quantifying the defect-mediated energy transfer efficiency as a function of nanocrystal size and reaction time, we determined that the radiative defect sites in ZnO are located between the nanocrystal core and surface (i.e., near surface sites) and the distance between the defect sites and the surface increases as the nanocrystals grow larger. The all-optical energy transfer approach represents a non-destructive characterization method to determine the spatial distribution of defects in semiconductor nanocrystals. The defect distributions can be correlated with optoelectronic or photocatalytic properties to elucidate structure/function relationships in a wide range of applications that involve light-matter interactions.

ACKNOWLEDGEMENTS

I would like to thank my family and friends for their support and encouragement throughout my graduate studies. I would also like to thank my advisor Justin Sambur for all of the guidance he provided me over the course of this project. I would like to thank my group members for all of their help, and my committee members for their support in reading this document.

TABLE OF CONTENTS

ABSTRACT.....	ii
ACKNOWLEDGEMENTS.....	iii
AN INTRODUCTION TO ENERGY TRANSFER.....	1
Energy Transfer Between Molecules.....	1
Energy Transfer Between Nanoparticles and Molecules.....	4
Defect-Mediated Energy Transfer	6
PROBING BURIED DEFECTS IN ZINC OXIDE NANOPARTICLES USING DEFECT-MEDIATED ENERGY TRANSFER.....	8
1. Introduction	8
2. Experimental Methods.....	10
3. Results	12
4. Discussion.....	25
5. Conclusions	27
FUTURE OUTLOOKS	28
Achieving 100% Efficient Energy Transfer	28
Probing Defect Identities	28
REFERENCES	30
APPENDIX.....	33

AN INTRODUCTION TO ENERGY TRANSFER

Energy transfer is a process that occurs between two species, referred to as the donor (D) and the acceptor (A). Specifically, energy transfer is the transfer of the excited state of the donor to the ground state of the acceptor:



where D^* represents the donor in the excited state, A represents the acceptor in the ground state, D represents the donor in the ground state, A^* represents the acceptor in the excited state, and k_r is the rate of resonance energy transfer.¹ This interaction depends on several factors, most importantly that the emission spectrum of the donor must overlap with the absorption spectrum of the acceptor.

This chapter will start with the underlying fundamentals necessary to understand energy transfer, and then focus on a specific type of energy transfer that occurs between nanoparticle donors and molecular acceptors.

Energy Transfer Between Molecules

Energy transfer can be radiative or nonradiative. In radiative energy transfer, the donor enters the excited state via photon absorption and relaxes by emitting a photon, which is then absorbed by the acceptor. The acceptor then enters the excited state and relaxes back down to the ground state by emitting a second photon. In nonradiative energy transfer, the donor does not emit

a photon for the acceptor to absorb. Instead, the acceptor becomes excited by the transfer of a bound exciton from the donor. One specific type of nonradiative energy transfer that is important to understand for this work is Förster Resonance Energy Transfer (FRET).

The FRET mechanism of energy transfer was first described by Theodor Förster in a series of papers published between 1946 and 1949.^{2,3} The FRET model describes a nonradiative energy transfer process from a molecular donor to a molecular acceptor as the result of long-range dipole-dipole interactions. The model defines the Förster distance as the distance at which FRET efficiency is 50%. The rate of FRET is given by:

$$k_T(r) = \frac{Q_D \kappa^2}{\tau_D r^6} \left(\frac{9000 \ln(10)}{128 \pi^5 N_A n^4} \right) \int_0^\infty F_D(\lambda) \epsilon_A(\lambda) \lambda^4 d\lambda \quad (2)$$

where Q_D is the quantum yield of the donor in the absence of the acceptor, τ_D is the fluorescence decay lifetime of the donor alone, r is the physical distance between the donor-acceptor pair, N_A is Avogadro's number, n is the refractive index of the medium, F_D is the fluorescence intensity from λ to $\Delta\lambda$, ϵ_A is the molar absorptivity of the acceptor, and κ^2 describes the relative orientations of the donor and acceptor.¹ κ^2 is usually assumed to be 2/3, which is derived from dynamic random averaging of the donor and acceptor.

Equation (3) relates the rate of FRET to the decay lifetime of the donor, the distance between the donor and acceptor, and the Förster distance, R_0 :

$$k_T(r) = \frac{1}{\tau_D} \left(\frac{R_0}{r} \right)^6 \quad (3)$$

The Forster distance is defined as the donor-acceptor distance at which FRET becomes 50% efficient. The efficiency of FRET is given by:

$$E = \frac{k_T(r)}{\tau_D^{-1} + k_T(r)} \quad (4)$$

Equations (2), (3), and (4) show that several factors can affect FRET efficiency. To achieve efficient energy transfer, the spectral overlap of the donor and acceptor should be maximized, and the distance between them should be minimized. Donor-acceptor distance impacts FRET efficiency most due to its r^{-6} dependence. FRET's large dependence on distance makes it a useful tool for determining distances between molecules, and has been referred to as a "spectroscopic ruler".¹

While the FRET model describes energy transfer between molecules well, it has limitations for systems involving nanoparticles. The model describes energy transfer between a single donor and acceptor pair separated by a defined distance r , which does not accurately reflect a mixture of nanoparticles and molecular acceptors in solution. Many of the equations derived for FRET assume that the fluorescence decay of the donor is single-exponential, which is often not the case for nanoparticles. Lastly, for most calculations using the FRET model, the quantum yield of the donor must be known. This can be difficult for nanoparticle systems because accurately calculating nanoparticle concentration requires a known molar absorptivity, which is different for different sizes and types of nanoparticles.⁴ Thus, a better model to describe energy transfer between nanoparticles and molecules is necessary.

Energy Transfer Between Nanoparticles and Molecules

Because nanoparticles behave differently from molecules, a better model for energy transfer between nanoparticles and molecules is required. Sadhu and coworkers described this interaction in 2009 using CdS nanocrystal donors.⁵ To do so, they synthesized CdS quantum dots (QDs) and quantum rods (QRs) and used Nile Red as a fluorescent acceptor molecule. They measured the steady-state emission of the QDs and QRs alone and in the presence of Nile Red in three concentrations to determine the quenching behavior of the CdS. They calculated the energy transfer behavior of the CdS using equation (5)

$$\Phi_{ET} = 1 - \frac{I}{I_0} \quad (5)$$

where I_0 is the initial integrated intensity of the CdS in the absence of dye, and I is the integrated intensity of the CdS/Nile Red mixture at a given concentration. To confirm that the changes in photoluminescence (PL) intensities of the CdS and the dye were due to energy transfer, they measured time-resolved photoluminescence of the QDs or QRs in the absence and presence of Nile Red. They derived the decay behavior from the following equations:



where QD_n (QD_n^*) is a quantum dot in the ground (excited) state, n is the number of dye molecules adsorbed, k_0 decay constant of the QD in the absence of the acceptor, and k_q is the rate of energy transfer per dye molecule.

The authors assumed that the number of dye molecules adsorbed to the QDs followed a Poisson distribution such that

$$\phi(n) = \exp(-m) * \frac{m^n}{n!} \quad (8)$$

where m is the mean number of dye molecules adsorbed to one QD. The excited-state decay of the QDs with m dye molecules then becomes

$$I(t, m) = I_0 \exp[-k_0 t - m(1 - \exp(-k_q t))] \quad (9)$$

The authors fit their time-resolved PL data to equation (9)(9) and found that the data collected at very early times did not fit well to the model. They attributed this behavior to nonradiative trap states in the QDs. They assumed that the trap states followed a Poisson distribution, and modified equation (9) to include these trap states:

$$I(t, 0) = I_0 \exp[-k_0 t - m_t(1 - \exp(-k_{qt} t))] \quad (10)$$

where m_t is the mean number of nonradiative traps and k_{qt} is the quenching rate due to nonradiative trap states. The decay in the presence of dye then becomes:

$$I(t, m) = I_0 \exp[-k_0 t - m_t(1 - \exp(-k_{qt} t)) - m(1 - \exp(-k_q t))] \quad (11)$$

The authors fit their data with equations (10) and (11) and were able to extract rates of energy transfer and determine the number of dye molecules adsorbed per QD in their solutions.

Their fits were in good agreement with their data. Their stochastic model has been used to describe many nanoparticle systems, including systems where the emission processes originate from shallow defect states, called defect-mediated energy transfer.

Defect-Mediated Energy Transfer

Defect-mediated energy transfer is an energy transfer process that happens at a defect site in the lattice of a nanocrystal. Molecular acceptors selectively interact with these defects, making defect-mediated energy transfer a useful tool for probing defect sites. Several groups have demonstrated defect-mediated energy transfer, but an example most closely related to this work is that of Beane and coworkers.⁶

Their work showed defect-mediated energy transfer between ZnO nanocrystals (NCs) and a commercially-available dye. ZnO is known for its defect-driven emission, which has been attributed to several species, including intrinsic⁷⁻¹¹ and extrinsic^{12,13} impurities. While there is much debate about the origin of ZnO's defect emission, many groups agree that oxygen vacancies are responsible.

Mulvaney and coworkers used steady-state and time-resolved PL spectroscopy to demonstrate that energy transfer between ZnO and adsorbed dye molecules is due to ZnO defect states, rather than the ZnO exciton state.⁶ They also found that a single dye molecule can quench the emission of a ZnO NC using the model described by Sadhu and coworkers.

Building off this study, my work describes the effects of ZnO NC size and photophysical properties on defect-mediated energy transfer. We prepared a size series of ZnO NCs and studied their energy transfer behavior relative to each other. Using time-resolved PL and the Sadhu model,

we calculated a donor-acceptor distance for each NC-dye system, and found that energy transfer does show a dependence on NC size.

PROBING BURIED DEFECTS IN ZINC OXIDE NANOPARTICLES USING DEFECT-MEDIATED ENERGY TRANSFER

1. Introduction

Semiconductor nanocrystals (NCs) are promising photocatalysts for solar fuels generation, environmental remediation, and fine chemical synthesis.¹⁴⁻¹⁶ The underlying processes in semiconductor photocatalysis are charge carrier generation, charge separation and transport, and interfacial charge transfer reactions. Charge carrier recombination is a competing process where photo-excited electrons and holes in the conduction and valence bands recombine radiatively or non-radiatively. Since semiconductor NCs have large surface-atom-to-volume ratios compared to bulk materials, electron-hole recombination often occurs at the particle surface because under-coordinated surface sites have electronic energy levels inside the semiconductor band gap (i.e., surface states). Defect-mediated electron-hole recombination at surface vacancies or impurity atoms is especially important for impure semiconducting materials such as solution-processed NCs; the solvents and reagents contain part-per-million or greater concentrations of impurities that can be incorporated into the material. While defect-mediated recombination in semiconductor NCs is widely recognized as a major challenge in a wide range of optoelectronic and solar energy conversion applications, it is generally challenging to characterize the identity and real-space position of surface defect sites on semiconductor NCs.

Characterizing the identity and position of defects in solids is challenging. Defect characterization requires methods that have atomic level chemical and spatial resolution. Scanning

probe microscope (SPM) methods such as atomic force microscopy and scanning tunneling microscopy have been used to characterize defects in solid materials.^{17–20} While SPM methods have been used to characterize defects in nanoscale materials, high-resolution SPM methods often require pristine flat surfaces in ultrahigh vacuum environments. Another approach to characterize defects in nanoparticles is atom probe tomography (APT). APT is a powerful analytical technique that allows for the 3D compositional mapping of materials with atomic resolution. However, APT is a destructive method that does not allow for one-to-one correlation for single particle-level structure/function relationship studies. High resolution electron microscopy (EM) is another real-space imaging approach to identify surface and bulk defect sites in nanocrystals. EM provides ultimate atomic-level spatial resolution. However, it is currently challenging to link the atomic-level structural properties as determined via EM to the (photo)catalytic properties of semiconductor NCs. The challenge stems from the fact that EM characterization requires that NC samples are deposited on a transmission electron microscopy grid for imaging experiments. Thus, developing a non-destructive and label-free defect imaging approach that is also compatible with single particle-level (photo)catalytic activity characterization is highly desirable to determine structure/function relationships in semiconductor NCs.

Here we present, in a two-part study, a single molecule, single particle-level fluorescence microscopy approach to characterize defect sites in semiconductor NCs. Our single molecule fluorescence microscopy approach is based on imaging defect-mediated energy transfer events between semiconductor NCs and surface adsorbed fluorescent molecules. Mulvaney and coworkers first demonstrated ensemble-level defect-mediated energy transfer between ZnO NCs and a commercially-available dye from the AlexaFluor series.⁶ In this process, a UV light source excites the bandgap of ZnO NCs ($E_g = 3.3$ eV for bulk) and the photo-excited charge carriers relax

to defect levels within the semiconductor bandgap. Specifically, photo-excited electrons likely trap at defect levels associated with oxygen vacancies in the ZnO lattice. The trapped electrons radiatively recombine with valence band holes. The defect-mediated recombination process produces a broad emission in the visible range, typically between 450 to 650 nm. Thus, UV excitation of ZnO NCs produces a visible emission peak due to energy levels inside the semiconductor bandgap (i.e., surface states).

Zinc oxide is an ideal model system with well-characterized defects to probe this problem. ZnO is a wide bandgap semiconductor with UV absorption bands and a visible emission.²¹ The visible emission stems from defects within the bandgap of the material. While the identities of these defects are still highly debated, their most likely assignment is oxygen vacancies.^{22,23}

In this study, we demonstrate the effects of size and photophysical properties of ZnO NCs on defect-mediated energy transfer with an AlexaFluor dye. We synthesized a size series of ZnO NCs and used steady-state PL to characterize the energy transfer properties of the samples. We also used time-resolved PL to describe the kinetics of the energy transfer process, which allowed us to calculate donor-acceptor distances for each NC-dye pair.

2. Experimental Methods

2.1 ZnO Nanocrystal Synthesis and Characterization.

ZnO nanocrystals (NCs) were synthesized using a base hydrolysis of Zn(II) in ethanol using an adapted procedure by Beane et al.⁶ In a typical reaction, 0.5054 g $\text{Zn}(\text{OAc})_2 \cdot 2\text{H}_2\text{O}$ (Sigma Aldrich) was added to 50 mL 200 proof ethanol (Pharmco-Aaper) in a 100-mL 3-neck round bottom flask. The solution was stirred with a stir plate and heated to 70 °C using a heating mantle and a temperature probe. Once the solid dissolved, 1 mL of tetramethylammonium hydroxide

(Sigma Aldrich) was added to the flask. We define the base injection step as $t = 0$ for this time-dependent nanocrystal growth procedure. 3-mL aliquots of the solution were extracted from the flask at growth times ranging from $t = 2$ to $t = 300$ min. Each aliquot was diluted to a total volume of 10 mL and stored at -4 °C when not in use. All reagents were used as received and without further purification.

2.2 Nanocrystal Characterization.

The nanocrystal samples were characterized with UV-Vis absorption spectroscopy (HP 8452A Diode Array Spectrophotometer) and electron microscopy (JEOL JEM-2100F Transmission Electron Microscope on copper grids with a carbon support Pelco, Ted Pella). Steady-state photoluminescence spectra were measured in 1 cm pathlength quartz cuvettes using a Horiba Jobin-Yvon FluoroLog-3 Spectrofluorometer. A 3D excitation/emission scan was measured for each sample to determine the maximum excitation wavelength ($\lambda_{\text{max,exc}}$). Time-resolved photoluminescence measurements were obtained using an Edinburgh Instruments FS5 Spectrofluorometer with a 150 W Xenon lamp for steady-state measurements and Edinburgh Instruments pulsed LEDs (EPLLED) for lifetime measurements.

2.3 Energy transfer measurements.

All energy transfer (EnT) measurements were performed with nanocrystal samples whose optical densities (ODs) were adjusted to either 0.1 or 0.01 at their first exciton peak, as measured by UV-Vis spectroscopy. 1 mL of each pre-diluted sample was diluted into 19 mL of ethanol for a total volume of 20 mL. In a typical EnT experiment, 5 μM ethanolic AlexaFluor 555 carboxylic acid dye (A555; Thermo Fisher) was injected into 2 mL of ZnO NC sample, yielding a bulk solution concentration $[\text{A555}] = 100$ nM . Each sample was excited at $\lambda_{\text{max,exc}}$ for the defect

emission peak to measure steady-state PL spectra of the A555 acceptor in the presence of the donor (ZnO). For time-resolved photoluminescence measurements, ethanolic solutions containing 100 nM A555 in 2 mL of 0.1 OD ZnO were excited with a pulsed 320 nm LED and the PL decay was detected at the ZnO defect peak maximum ($\lambda_{\text{max,em}}$). The PL lifetime of the donors (ZnO NCs) and acceptor (A555) were measured with 340 nm and 532 nm pulsed LEDs, respectively.

3. Results

3.1 Size-dependent optical properties of ZnO NCs.

We prepared a series of ZnO NC samples to study how NC size and photophysical properties influence EnT efficiency. The NCs were synthesized from a base hydrolysis reaction of zinc acetate in ethanol. In a typical reaction, we initiate NC growth by injecting tetramethylammonium hydroxide into a zinc acetate solution that was maintained at 70 °C. Figure 1a shows a series of absorbance spectra from aliquots that were isolated from the reaction flask as a function of reaction time. At $t = 2$ min following the injection step, the absorbance spectrum shows a peak at 327 nm that is consistent with the excitonic absorption peak of ZnO NCs. The excitonic peak shifts to longer wavelengths with increasing reaction time, which is in agreement with literature reports that the quantum-confined ZnO NCs increase in size under these reaction conditions.²² At long reaction times ($t > 120$ min), a significant absorption offset and tail feature appears for $\lambda > 375$ that can be attributed to particle aggregation; the tail feature disappears after a post-synthesis washing and sonication procedure (SI Figure 1).

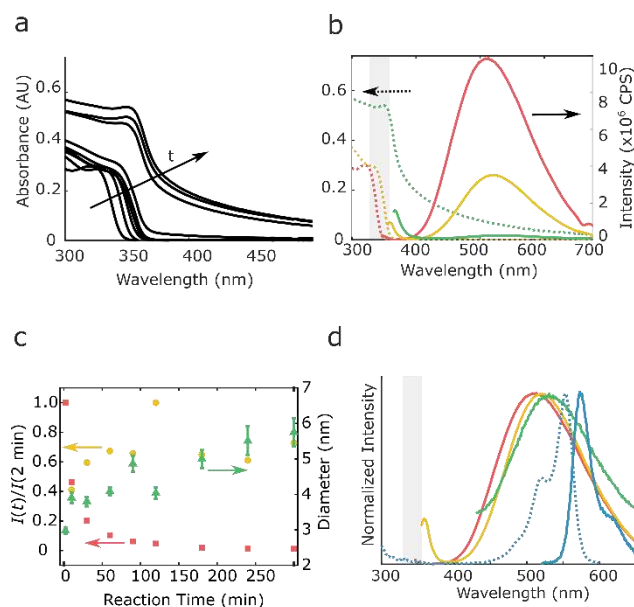


Figure 1. Optical properties of ZnO samples. (a) UV-Vis absorbance spectra of ZnO NCs in ethanol as a function of reaction time. The shortest and longest reaction times were 2 min and 300 min. (b) Absorbance (dashed traces) and emission (solid traces) spectra of ZnO samples that were isolated at 2 min (red traces), 30 min (yellow traces), and 180 min (green traces). (c) Normalized defect emission intensity (red squares) and NC diameter (green triangles) as a function of reaction time. (d) Normalized emission spectra of 2 min ZnO (red), 30 min ZnO (yellow), 180 min ZnO (green) NCs compared to the excitation and emission spectrum of the A555 dye (dashed blue: excitation, solid blue: emission).

We compared the photoluminescence properties of the ZnO NCs that were isolated at different reaction times. To do so, we adjusted the optical density (OD) of the NC solutions to ~ 0.1 at the half-maximum of the first exciton peak. The OD adjustment allows us to compare the absolute emission of the ZnO NC samples under similar NC concentration conditions. We note that at the same optical density, the largest ZnO sample is about 4 times more dilute than the smallest ZnO sample. We roughly calculated this ratio based on the average surface area of each particle. Figure 1b compares the photoluminescence (PL) spectra of the 2 min, 30 min, and 180 min ZnO NC samples in ethanol. All the NC samples exhibit an emission peak in the UV range (< 400 nm) and a relatively broad emission peak at 500 nm. The emission peaks can be assigned to radiative conduction band-to-valence band recombination (or bandgap emission) and defect-

mediated recombination (or defect emission), respectively. Figure 1c summarizes how the defect emission and NC diameter (as determined by TEM analysis) change with increasing reaction time. The defect emission intensity decreases by a factor of approximately 40, while the NC diameter increases by a factor of two. We note that all PL spectra were measured by exciting the NC samples at the peak excitation wavelength of the defect emission peak to best compare the NC size-dependent defect emission intensity. While the defect emission decreases with reaction time, the bandgap emission intensity increases with reaction time (Figure 1c) The significant decrease in defect emission and increase in bandgap emission suggests that either longer growth times decrease defect concentrations in these ZnO NCs or the kinetics of band-to-band recombination out-competes the defect-mediated recombination process. The emission intensity changes are likely not due to concentration differences between the solutions because the defect PL intensity decreases by more than an order of magnitude but the NC diameter and therefore optical cross section increases by a factor of four. That is, it is reasonable to assume that the small variation in NC concentrations in these OD-normalized experiments cannot account for the large variation in emission properties among the different NC samples.

The defect emission peak shifts to longer wavelengths (21 nm) with increasing particle size as shown in Figure 1d. van Dijken et al observed a similar effect whereby the defect emission peak shift is small compared to the first exciton absorption peak shift.²² In that study, the authors attributed the effect to a pinned defect energy level inside the NC bandgap. In this scenario, the defect emission peak shifts to lower energy with increasing NC size because the ZnO conduction band edge constantly shifts to lower energy while the defect level inside the ZnO bandgap is fixed. In summary, the (1) the particle diameter increases by a factor of 2, (2) the defect emission intensity

decreases by a factor of 40, (3) the bandgap emission increases by a factor of 2, and (4) the defect PL peak shifts to slightly lower energy with increasing reaction time.

Since the broad defect emission peak shows a slight red shift with increasing particle size, we explored whether all ZnO NC samples studied herein could be used as energy transfer donors to the same molecular acceptor. Following Mulvaney and co-workers, we explored AlexaFluor 555 carboxylic acid dye (A555) as an acceptor.⁶ Figure 1d shows the normalized defect emission spectra of the smallest and largest ZnO NC donors compared to the absorption spectrum of the A555 acceptor. The defect emission of all NC donors overlaps significantly with the absorption spectrum of A555. Thus, we expect to observe defect-mediated EnT between all ZnO NC donors and A555 acceptors.

3.2 Size-dependent defect-mediated energy transfer behavior: steady-state PL measurements.

We studied defect-mediated EnT between ZnO NC donors and AlexaFluor 555 carboxylic acid dye (A555) molecular acceptors using steady-state fluorescence spectroscopy. In a typical EnT experiment, we perform control experiments by photo-exciting ethanol solutions containing only ZnO NCs or A555 with UV light (340-355 nm). This UV excitation range corresponds to the maximum ZnO defect excitation wavelength and a minimum A555 fluorescence wavelength (see dye excitation spectrum in Figure 1d). Then, we probe defect-mediated EnT behavior by photo-exciting ZnO NC solutions in the presence of the A555 dye. Figure 2a shows representative energy transfer measurements of ZnO-2 min (2.97 nm diameter) as a function of bulk A555 concentration. The ZnO defect emission intensity at 513 nm decreases and the dye fluorescence intensity at 575 nm increases with increasing bulk A555 concentration (Figure 2b). The spectral changes in Figure

2a-b are consistent with defect-mediated EnT: the donor emission intensity decreases and the acceptor emission intensity increases in mixture solutions that contain both donor and acceptor. In this particular ZnO NC solution, the defect emission intensity is almost completely quenched for $[A555] > 300$ nM (Figure 2b, red squares). The A555 fluorescence intensity at 575 nm increases rapidly and then saturates for $[A555] > 200$ nM (Figure 2b, yellow circles).

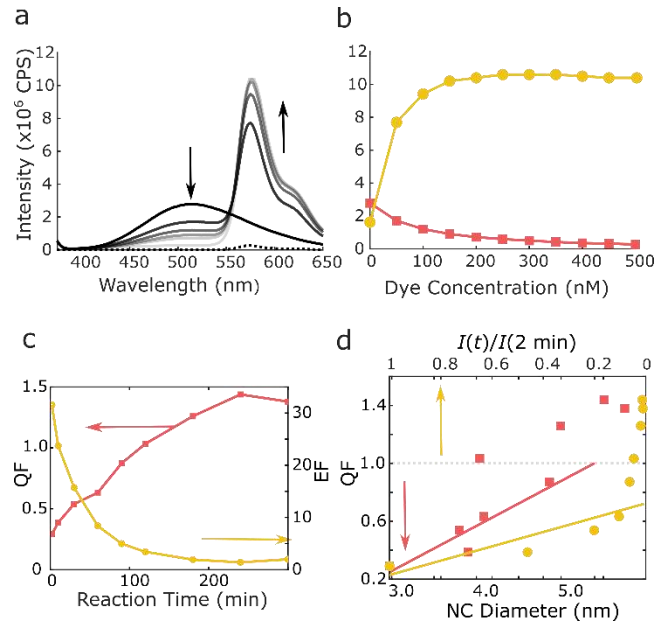


Figure 2. Size-dependent defect mediated energy transfer behavior via steady state PL measurements. **a)** Steady-state PL spectra of 2.97 nm ZnO NCs in ethanol (solid black line) and in the presence of increasing concentrations of A555 dye. The dashed black line represents 100 nM A555 in ethanol. All samples were excited at 345 nm. The black arrows indicate that the A555 emission at 575 nm increases and the ZnO defect PL emission at 513 nm decreases with increasing A555 concentration. **b)** ZnO defect PL intensity (red squares) and the A555 fluorescence intensity (yellow circles) versus bulk dye concentration from the spectra in (a). **c)** Defect quenching (red squares, left axis) and dye enhancement (yellow circles, right axis) factors versus reaction time. The data were calculated according to Eqs. (12) and (13) in the main text. **d)** Quenching factor versus NC diameter (red squares) and normalized defect emission (yellow circles). Solid lines represent linear fits to the QF data < 1 ; we neglect the anomalous quenching behavior as described in the main text.

Next, we studied the ZnO defect PL quenching and A555 fluorescence enhancement as a function of reaction time (i.e., particle size). We quantified the defect PL quenching factor (QF_{ZnO}) and dye fluorescence enhancement factor (EF_{A555}) at a fixed NC optical density (0.01) and dye concentration (100 nM) according to Eqs. (12) and (13), respectively. QF_{ZnO} represents the ratio of the defect PL intensity of ZnO NCs in the presence and absence of A555 (I_{mix} versus I_{ZnO} , respectively). EF_{A555} represents the ratio of the A555 fluorescence in the presence and absence of ZnO. Since the ZnO defect emission overlaps with the A555 fluorescence signal, we subtract the ZnO defect emission intensity at 575 nm from the ZnO/dye mixture at 575 nm to calculate EF_{A555} . The 0.01 OD condition was chosen because we observed less NC aggregation for lower OD solutions (SI Figure 5). The 100 nM condition was chosen because it was the maximum allowable concentration that did not saturate the fluorescence spectrometer detector for all NC samples studied herein. That is, the dye concentration that is required to observe full quenching for the smallest NCs (longest reaction time) at 0.01 OD saturates the detector.

$$QF_{NC} = \frac{I_{mix,Defect\ Em}}{I_{ZnO,Defect\ Em}} \quad (12)$$

$$EF_{dye} = \frac{I_{mix,\lambda=575} - I_{ZnO,\lambda=575}}{I_{A555,\lambda=575}} \quad (13)$$

Figure 2c shows QF_{ZnO} (red squares, left axis) and EF_{A555} (yellow circles, right axis) versus reaction time (i.e., increasing NC size). QF_{ZnO} is smallest (0.3) for the shortest reaction time (2.97 nm diameter) and it increases monotonically with reaction time. We note that QF_{ZnO} approaches 0.0 for the same 2.97 nm sample in the presence of 500 nM A555 (Figure 2b). $QF_{ZnO} > 1$ indicates that the defect emission of the mixture solution is greater than ZnO alone; the ZnO defect peak is not quenched in the presence of A555. EF_{A555} shows the opposite trend: EF_{A555} is 32 for the shortest

reaction time and it decreases monotonically with reaction time. $EF_{A555} > 1$ indicates that A555 fluorescence is enhanced in the presence of ZnO NCs. Interestingly, $EF_{A555} > 1$ and $QF_{ZnO} > 1$ for longer reaction times (>125 min). The fact that both factors exceed unity indicates that the acceptor emission is enhanced even though the donor emission is not quenched (see SI Figure 5).

Here we discuss possible origins of the increase in steady-state PL intensity of the ZnO defect emission peak in the presence of 100 nM A555 ($QF_{ZnO} > 1$). One possibility is that adsorbed A555 molecules or counter ions from the injected dye solution bind to ZnO surface sites that contribute to non-radiative electron-hole recombination. In this scenario, the adsorbates passivate non-radiative recombination sites by either removing the energy level from the ZnO bandgap or occupying the vacant level.²⁴ Thus, the adsorbates remove non-radiative recombination pathways and therefore promote radiative defect-mediated recombination. This hypothesis is supported by the fact the defect PL intensity of these ZnO NCs increased in the presence of excess formate (SI Figure 4). Another possibility is that the injected dye solution promotes separation of ZnO NC aggregates. We observed significant NC aggregation for the longest reaction times (Figure 1a) and it is possible that the defect PL of individual NCs is quenched in the aggregate structure. The dye injection step could separate individual NCs from the aggregates and increase overall defect PL intensity. This ZnO aggregation hypothesis is supported by the fact that the anomalous EnT behavior is more pronounced in more concentrated ZnO solutions (e.g., 0.1 OD in SI Figure 5). Lastly, it is possible that EnT occurs via dark ZnO defect states. In this scenario, mid-gap electronic states that contribute to non-radiative recombination in ZnO NCs transfer energy to surface adsorbed dyes. The NC defect emission is relatively unaffected even though the acceptor emission increases. Regardless of the underlying mechanism, the steady-state PL data at a fixed NC optical density (i.e., concentration) indicates that EnT efficiency decreases with reaction time.

Since the NC photophysical properties and size both scale differently with reaction time (Figure 1c), we explored whether the reaction time-dependent EnT behavior is more strongly correlated with the defect emission intensity or the NC diameter. Figure 2d compares QF_{ZnO} versus the normalized defect emission intensity (yellow circles) and the NC diameter (red squares). For QF_{ZnO} values < 1 , corresponding to EnT behavior where the donor emission is quenched, QF_{ZnO} is more strongly correlated with NC diameter than defect emission intensity. The stronger correlation with NC diameter is evidenced by a Pearson correlation coefficient of $\rho = 0.91$ versus -0.76 in Figure 2d (solid line fits for QF_{ZnO} values < 1). Since the ZnO defect quenching scales more strongly with physical properties, we hypothesized that this could be due to a change in the donor-acceptor distance as a function of reaction time. In the following section, we explore the EnT efficiency as a function of donor-acceptor distance as determined by time-resolved PL measurements.

3.3 Size-dependent defect-mediated energy transfer behavior: time-resolved PL measurements.

Here we quantify defect-mediated EnT behavior using time-resolved PL measurements. For these experiments, a pulsed 340 nm LED excited the control or mixture samples and the PL intensity decay at the defect emission peak was measured as a function of time. Figure 3 shows the defect emission decay at $\lambda_{\max, \text{defect}}$ for the 2 min, 30 min, and 180 min ZnO NC samples in the absence and presence of A555 acceptors. The PL decay kinetics of the ZnO NCs in ethanol did not follow single exponential kinetics. Instead, following Mulvaney and co-workers, we fit the decay kinetics of the ZnO NCs alone using equation (14).⁶ Equation (14) assigns the fast PL decay component to non-radiative quenching by trap states, where λ_t is the number of trap states per nanocrystal and k_{qt} is the quenching rate. The slow PL decay radiative process decays at a rate k_0 .

The solid black line fits to the ZnO alone data (red circles) in Figure 3 indicate that Equation (14) describes the PL decay dynamics of these ZnO NCs.

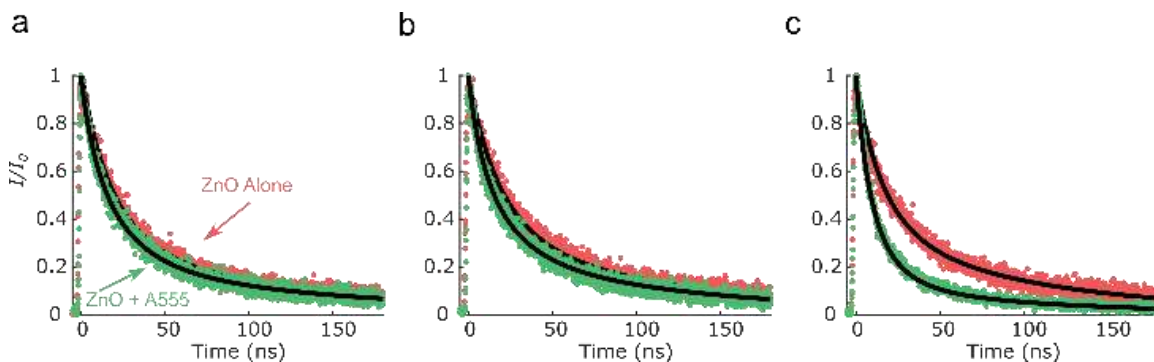


Figure 3. Time-resolved energy transfer. (a-c) Time-resolved PL of (a) 2 min, (b) 30 min, and (c) 180 min ZnO NC samples (0.01 OD) in ethanol (red circles) and in the presence of 100 nM A555 (green circles). The solid black lines represent fits according to equations (14) and (15) for the ZnO alone and ZnO/dye samples, respectively.

$$\frac{I}{I_0} = \exp(-k_0 t - \lambda_t(1 - \exp(-k_{qt} t))) \quad (14)$$

Figure 4a shows k_0 (yellow circles) and k_{qt} (red squares) for the 2, 30, and 180 min ZnO samples in ethanol. The fit parameters are tabulated in SI Table 1. The rates of radiative defect emission (k_0) and quenching due to trap states (k_{qt}) are independent of reaction time. Moreover, the average number of non-radiative traps per NC decreases by about 15% for the 180 min samples. Since k_0 and k_{qt} are independent of reaction time but λ_t decreases with increasing reaction time, it could be expected that the defect PL for the 180 min samples would be greater than the 2 min samples. However, Figure 1b shows that the defect PL quantum yield (QY) of the 180 min samples are about an order of magnitude lower than the 2 min samples. To rationalize the reaction time-independent k_0 and k_{qt} values as well as the decreasing defect PL QY with increasing reaction time,

we hypothesize that the average number of radiative defect levels per NC decreases significantly with increasing reaction time. Thus, the total number of mid-bandgap levels decreases, but the radiative defect levels decrease much more than the non-radiative defect levels. This hypothesis is supported by the increase in bandgap PL versus reaction time (Figure 1c).

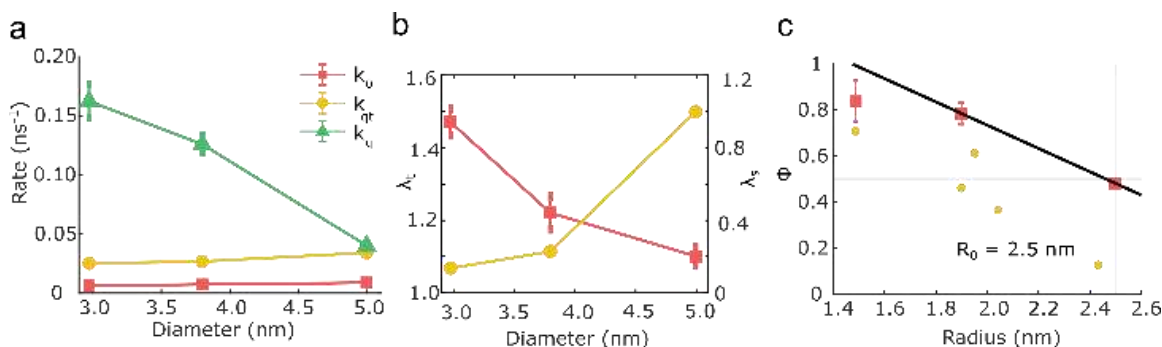


Figure 4. Energy transfer analysis. (a) Rate of energy transfer (green triangles), rate of radiative decay of the ZnO defect state (yellow circles), quenching rate of the nonradiative trap states in ZnO (red squares) as a function of particle diameter. (b) Mean number of nonradiative trap sites per ZnO NC (red squares) and the mean number of A555 molecules adsorbed per ZnO NC (yellow circles) as a function of NC diameter. (c) Energy transfer efficiency of ZnO NCs in the presence of A555 as a function of particle diameter (red squares). The black line represents a fit of the linear portion of the curve to extrapolate R_0 .

The defect PL intensity of the ZnO NCs decays faster in the presence of the A555 acceptor molecules (Figure 3a-c, green circles). The ZnO NC bandgap PL dynamics showed no significant difference in the presence of A555 (SI Figure 6). Therefore, we conclude that energy transfer occurs via defect energy states. Following Tachiya and Mulvaney, we fit the defect PL decay curves of the ZnO/dye mixtures using equation (15), where λ_s is the mean number of dye molecules adsorbed to the NC surface and k_q is the rate of defect-mediated energy transfer.^{5,6} The model considers that energy transfer proceeds via one or more NC defects to a molecular acceptor.⁵ The model also assumes that the surface coverage of dye molecules follows a Langmuir adsorption isotherm and the distribution of dye molecules among the NCs follows a Poisson distribution. We

fit equation (15)(15) to the ZnO/dye data by fixing k_0 , k_{qt} , and λ_t that were determined from the ZnO NC samples in ethanol; λ_s and k_q are the only adjustable parameters for the ZnO/dye data.

$$\frac{I}{I_0} = \exp(-k_0 t - \lambda_t(1 - \exp(-k_{qt} t)) - \lambda_s(1 - \exp(-k_q t))) \quad (15)$$

The rate of energy transfer from defect states to dye acceptors (k_q) decreases with increasing reaction time (green triangles, Figure 4a) even though the mean number of adsorbed dye molecules per NC increases (Figure 4b, right axis, yellow). The dye surface coverage likely increases because the number of NC binding sites increases as the particle diameter increases and we fixed the bulk solution dye concentration and NC optical density across all experiments. Thus, we expect that the 180 min ZnO sample contains less particles than the 2 min samples and therefore a greater dye:NC ratio. Next, we calculated the energy transfer efficiency (ϕ) according to equation (16) for the time resolved data and equation (17) for the steady state PL data:

$$\phi_{tr} = \frac{k_q}{k_0 + k_q + k_{qt}} \quad (16)$$

$$\phi_{ss} = 1 - QF_{ZnO} \quad (17)$$

Figure 4c shows that the energy transfer efficiency decreases as NC size increases. The ϕ values calculated according to equation (16) plateau at 0.8 for the 1.5 and 1.9 nm NCs (2 and 30 min reaction time) and then ϕ decreases to 0.55 for the 2.0 nm NC (180 min reaction time). The ϕ values calculated according to equation (17) show the same general trend, but the values determined from the steady state PL data are lower than the time-resolved values. The ϕ values determined via trPL measurements and equation (16)(16) take into account that EnT occurs via

one or more NC defects whereas the values determined from steady state PL measurements and equation (17) only consider EnT via a fixed donor-acceptor distance. The abrupt decrease in ϕ with increasing particle size suggests that EnT decreases due to an increase in the donor-acceptor distance. This hypothesis is supported by the fact that the energy transfer rate k_q depends sensitively on donor-acceptor distance according to equation (18):

$$r = \sqrt[6]{\frac{R_0^6 - \phi R_0^6}{\phi}} \quad (18)$$

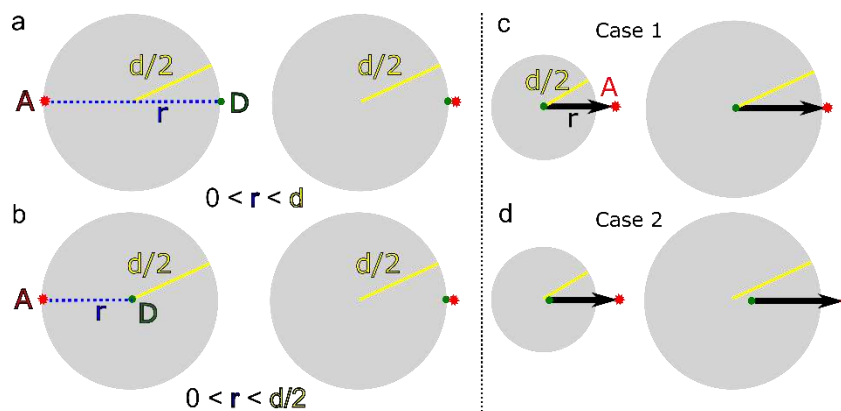
In the following sections, we discuss how the donor-acceptor distance r could change as a function of reaction time. First, we first consider a range of possible r values in Scheme 1. The maximum possible r corresponds to the situation where the defect site is located at the NC surface and the acceptor molecule adsorbs on the opposite side of the NC; the donor-acceptor pair is separated by the particle diameter (Scheme 1a, left). On the other hand, the minimum possible r corresponds to the situation where the dye molecule adsorbs directly to a surface defect site (Scheme 1a, right). In this direct adsorption case, the observed r value represents the extension of the fluorophore from the NC surface. Thus, there are two contributions to r : (1) the distance between the defect site and the NC surface, and (2) the extension of the fluorophore from the surface.

To estimate how r changes as a function of reaction time, we consider that our ensemble-level measurements do not probe the maximum and minimum r situations described above because those situations occur only for a particular surface dye binding motif. Instead, we consider that the surface adsorbed dye molecules bind randomly to all NC surface sites. If we consider that the ensemble-average measurements sample many possible defect/dye separation distances, then the

maximum r value most likely corresponds to the situation where the defect site is located in the center of the NC and the dye molecule is located on the surface (Scheme 1b). The maximum donor-acceptor distance in this geometry is the particle radius ($d/2$). To calculate r according to equation (18), we first estimated the Forster distance R_0 , or the donor-acceptor distance at which $\phi = 50\%$,¹ by assuming the donor-acceptor configuration in Scheme 1. We chose to determine R_0 using the trPL-derived ϕ values instead of the steady state PL-derived values because the trPL analysis was developed for a NC donor and molecular acceptor. We calculated an R_0 value of 2.5 nm by linearly interpolating the particle diameter at which $\phi = 0.5$ (Figure 4c). The R_0 value for these ZnO NC donor/A555 acceptor pairs is on the same order of magnitude as the R_0 values reported for AlexaFluor donor-acceptor pairs.²⁵

Having estimated R_0 for these ZnO NC donor/A555 acceptor pairs, we used equation (18) to estimate r so that we could relate NC size and energy transfer behavior. This calculation incorporates the size dependent defect PL lifetime of the ZnO NCs. We found that r increases with increasing reaction time, and is larger than $d/2$ for all samples. We consider two possible defect placement scenarios, which are summarized in Scheme 1c-d. Case 1 (Scheme 1c) assumes that the defect that undergoes energy transfer is in the core of the particle. In this case, the acceptor is positioned off the surface of the NC for the smallest NCs, and on the surface of the largest NCs. However, we know that the dye interacts with the NC by binding to the surface of the NC via a carboxylic acid functional group, which means the fluorophore (or energy transfer acceptor) of the dye molecule must be some distance away from the NC surface. Thus, it is unlikely that, on average, the defects are located at the NC core. Instead, if we assume that r is a vector with one end positioned at the centroid of the acceptor and the other end positioned inside the NC, then the defects are positioned between the NC core and surface (i.e., at near surface sites in Scheme 1d).

In this picture, $\phi < 1$ for the smallest NC samples because not all radiative defect sites are located at the NC surface. ϕ and k_q decrease with increasing reaction time presumably because, on average, the defects move farther away from the NC surface as NC growth proceeds.



Scheme 1. Different cases of defect/dye placement based on particle radius and donor-acceptor distance. **(a)** Two extreme cases of donor and acceptor placement in a ZnO NC-A555 system, with the longest (left) and shortest (right) possible r where $0 < r < d$. The green circle represents the defect (donor) and the red star represents the fluorophore (acceptor). **(b)** Donor-acceptor placement where defects are located in the NC core and $0 < r < d/2$. **(c)** Case 1 of defect-dye placement where the defect is in the center of the NC, drawn to scale for the smallest (left) and largest (right) NCs in this study. The yellow line represents the particle radius, and the black arrow represents the donor-acceptor distance as calculated by Equation (18). **(d)** Case 2 of defect-dye placement where the defect is located between the particle surface and core, and the fluorophore is a set distance off the NC surface.

4. Discussion

Here we discuss the two major results of this study: (1) energy transfer behavior decreases as ZnO NCs grow larger, and it is possible to observe energy transfer in which both QF_{ZnO} and EF_{A555} exceed unity and (2) energy transfer efficiency starts near 1 and decreases to around 0.5 as NC diameter increases.

For QF_{ZnO} to be greater than one, the emission intensity of the defect must be greater in the presence of A555 than in the absence of it. As previously discussed, we believe this is due to

the de-aggregation of ZnO NC clusters either from adsorbed dye molecules or counter ions from the dye solution. However, the separation of clusters does not necessarily account for why energy transfer can take place even when $QF_{ZnO} > 1$ (i.e., when $QF_{ZnO} > 1$ and $EF_{A555} > 1$). We observe this phenomenon more frequently as NC diameter increases, as shown in Figure 1c.

One explanation for the observation of anomalous energy transfer as NC diameter increases is the increase in particle size distribution. As NCs grow for longer reaction times, the average particle size increases, and the overall size distribution broadens (see SI Figure 3). It is possible that only small NCs participate in energy transfer, and large NCs are inactive. The large NC samples contain a smaller population of “active” NCs than the early samples, and while the small NCs participate energy transfer (evidenced by $EF_{A555} > 1$), the large NC population continues to exhibit defect emission, resulting in $QF_{ZnO} \geq 1$.

Another possible cause of anomalous energy transfer is the presence of “dark states” which may grow in at longer synthesis times. These dark states are states that do not contribute to the visible defect emission, but can participate in energy transfer. Dark states have been theorized and observed in NC systems.^{26,27}

The second major finding of this study is that energy transfer efficiency decreases as NC diameter increases, as shown in Figure 4c. This behavior suggests that defect location within an NC changes as a function of reaction time. If the defects that participate in energy transfer are located on the surface of the NC, then the efficiency of energy transfer from those defects should be independent of NC diameter. Instead, we suggest that defects move away from the NC surface and closer to the NC core as synthesis time and NC diameter increase. The results shown here

indicate that energy transfer can be used as a tool to non-destructively probe even “buried” defects.

5. Conclusions

We studied size dependent energy transfer between ZnO NCs and AlexaFluor 555 acceptors. The energy transfer process proceeds via defect levels inside the ZnO NC bandgap and surface adsorbed dye molecules. Steady state and time-resolved PL measurements showed that defect-mediated energy transfer efficiency decreases with increasing particle size. Quantitative analysis of the energy transfer rate versus particle size provides insight into how the donor-acceptor distance changes during NC growth. For these NC donors, the defect donor sites are likely distributed between the NC core and surface. The average distance between defect sites and acceptor molecules increases with increasing reaction time. Thus, energy transfer measurements can provide insight into the spatial distribution of defects in semiconductor NCs. This all-optical characterization approach represents an attractive strategy to determine structure/function relationships in semiconductor NCs such as the correlation between defect concentrations and photocatalytic activity.

FUTURE OUTLOOKS

Achieving 100% Efficient Energy Transfer

One question left unanswered by this work is why we did not observe 100% efficient energy transfer even with our high quantum yield ZnO. Based on Figure 4c, energy transfer efficiency increases as particle size decreases. The smallest ZnO sample shown in this work had an average particle diameter of 2.97 nm, which was isolated after only 2 minutes of synthesis. It seems unlikely that synthesis times shorter than 2 minutes will be practical, limiting the minimum NC size using this method. However, synthesizing extremely small NCs may not be the only way to investigate 100% efficient energy transfer.

As previously stated, all NC samples are inherently heterogeneous. Studying NCs on the ensemble level obscures the behavior of individual NCs, which may or may not perform like the average of the sample. It is likely that there are some NCs within a sample that undergo 100% efficient energy transfer, but are lost in ensemble averaging. Thus, studying NC samples on the single-particle level could yield more insightful information about efficient energy transfer. By using fluorescence microscopy, one could immobilize NCs and study their optical properties as dye is added to the sample. Then, the optical images could be correlated to some other measurement technique such as SEM that is capable of resolving NC structure and morphology.

Probing Defect Identities

A major goal in studying defects in NC systems is being able to determine the chemical identity of the defects present. ZnO is hypothesized to contain several types of defects, all of which can theoretically participate in defect-mediated energy transfer. Currently there are no studies that use energy transfer to identify defects based on their chemical composition.

By changing the functional moiety of a fluorophore, one could use chemistry to identify defects based on their selective interactions with specific functional groups. The AlexaFluor dye used in this work is available with several different functional groups, which could potentially interact with the different possible defects in ZnO with different efficiencies. For example, you could expect the maleimide-modified version of a dye to be more selective for oxygen vacancies than a cadaverine-modified version because of maleimide's larger dipole moment. By screening ZnO NC samples with dyes composed of the same fluorophore with a different functional group, one could identify relative concentration(s) of the different type(s) of defects present in ZnO NCs.

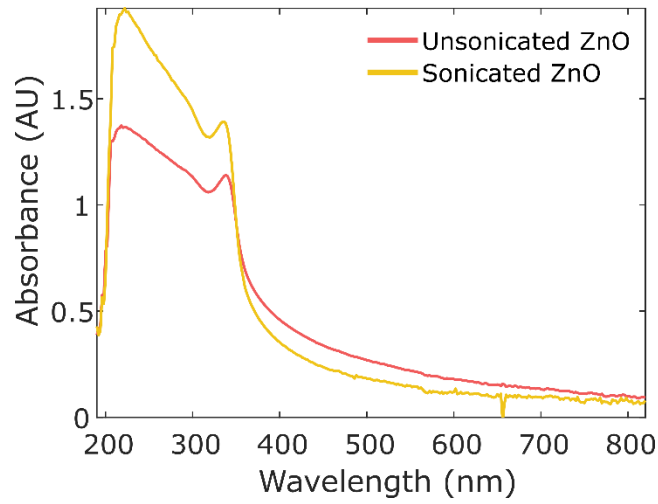
REFERENCES

- (1) Joseph R. Lakowicz. *Principles of Fluorescence Spectroscopy*, 3rd ed.; Springer eBook collection; Springer: New York ; Berlin, New York, 2006.
- (2) Forster, Th. Energiewanderung und Fluoreszenz. *Naturwissenschaften* **1946**, *33* (6), 166–175. <https://doi.org/10.1007/BF00585226>.
- (3) Förster, T. Zwischenmolekulare Energiewanderung und Fluoreszenz. *Ann. Phys.* **1948**, *437* (1–2), 55–75. <https://doi.org/10.1002/andp.19484370105>.
- (4) Jasieniak, J.; Smith, L.; van Embden, J.; Mulvaney, P.; Califano, M. Re-Examination of the Size-Dependent Absorption Properties of CdSe Quantum Dots. *J. Phys. Chem. C* **2009**, *113* (45), 19468–19474. <https://doi.org/10.1021/jp906827m>.
- (5) Sadhu, S.; Tachiya, M.; Patra, A. A Stochastic Model for Energy Transfer from CdS Quantum Dots/Rods (Donors) to Nile Red Dye (Acceptors). *J. Phys. Chem. C* **2009**, *113* (45), 19488–19492. <https://doi.org/10.1021/jp906160z>.
- (6) Beane, G. A.; Morfa, A. J.; Funston, A. M.; Mulvaney, P. Defect-Mediated Energy Transfer between ZnO Nanocrystals and a Conjugated Dye. *J. Phys. Chem. C* **2012**, *116* (5), 3305–3310. <https://doi.org/10/fz2frb>.
- (7) Mollwo, E. Die Wirkung von Wasserstoff auf die Leitfähigkeit und Lumineszenz von Zinkoxydkristallen. *Z. Für Phys.* **1954**, *138* (3), 478–488. <https://doi.org/10.1007/BF01340694>.
- (8) Smith, J. M.; Vehse, W. E. ESR of Electron Irradiated ZnO Confirmation of the F+ Center. *Phys. Lett. A* **1970**, *31* (3), 147–148. [https://doi.org/10.1016/0375-9601\(70\)90199-4](https://doi.org/10.1016/0375-9601(70)90199-4).
- (9) Kröger, F. A.; Vink, H. J. The Origin of the Fluorescence in Self-Activated ZnS, CdS, and ZnO. *J. Chem. Phys.* **1954**, *22* (2), 250–252. <https://doi.org/10.1063/1.1740044>.
- (10) van Dijken, A.; Meulenkamp, E. A.; Vanmaekelbergh, D.; Meijerink, A. The Kinetics of the Radiative and Nonradiative Processes in Nanocrystalline ZnO Particles upon Photoexcitation. *J. Phys. Chem. B* **2000**, *104* (8), 1715–1723. <https://doi.org/10/fdznp3>.
- (11) Vanheusden, K.; Seager, C. H.; Warren, W. L.; Tallant, D. R.; Voigt, J. A. Correlation between Photoluminescence and Oxygen Vacancies in ZnO Phosphors. *Appl. Phys. Lett.* **1996**, *68* (3), 403–405. <https://doi.org/10/c7vnr8>.
- (12) Dingle, R. Luminescent Transitions Associated With Divalent Copper Impurities and the Green Emission from Semiconducting Zinc Oxide. *Phys. Rev. Lett.* **1969**, *23* (11), 579–581. <https://doi.org/10.1103/PhysRevLett.23.579>.

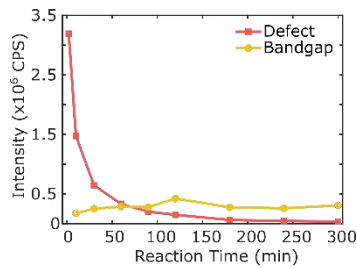
- (13) Craeynest, F. van; Vorst, W. M.-V. D.; Dekeyser, W. Interpretation of the Yellow Colour of Heat Treated ZnO Powder. *Phys. Status Solidi B* **1965**, 8 (3), 841–846. <https://doi.org/10.1002/pssb.19650080322>.
- (14) Jiang, D.; Wang, W.; Zhang, L.; Zheng, Y.; Wang, Z. Insights into the Surface-Defect Dependence of Photoreactivity over CeO₂ Nanocrystals with Well-Defined Crystal Facets. *ACS Catal.* **2015**, 5 (8), 4851–4858. <https://doi.org/10.1021/acscatal.5b01128>.
- (15) Ong, C. B.; Ng, L. Y.; Mohammad, A. W. A Review of ZnO Nanoparticles as Solar Photocatalysts: Synthesis, Mechanisms and Applications. *Renew. Sustain. Energy Rev.* **2018**, 81, 536–551. <https://doi.org/10/gcqcwz>.
- (16) Jagadale, T. C.; Takale, S. P.; Sonawane, R. S.; Joshi, H. M.; Patil, S. I.; Kale, B. B.; Ogale, S. B. N-Doped TiO₂ Nanoparticle Based Visible Light Photocatalyst by Modified Peroxide Sol–Gel Method. *J. Phys. Chem. C* **2008**, 112 (37), 14595–14602. <https://doi.org/10.1021/jp803567f>.
- (17) Giessibl, F. J. Atomic Resolution of the Silicon (111)-(7x7) Surface by Atomic Force Microscopy. *Science* **1995**, 267 (5194), 68–71. <https://doi.org/10/dtd6pf>.
- (18) Avouris, Ph.; In-Whan Lyo. Probing and Inducing Surface Chemistry with the STM: The Reactions of Si(111)-7 × 7 with H₂O and O₂. *Surf. Sci.* **1991**, 242 (1), 1–11. <https://doi.org/10/dd6kd3>.
- (19) Stolyarova, E.; Rim, K. T.; Ryu, S.; Maultzsch, J.; Kim, P.; Brus, L. E.; Heinz, T. F.; Hybertsen, M. S.; Flynn, G. W. High-Resolution Scanning Tunneling Microscopy Imaging of Mesoscopic Graphene Sheets on an Insulating Surface. *Proc. Natl. Acad. Sci.* **2007**, 104 (22), 9209–9212. <https://doi.org/10/fqzrf2>.
- (20) Takahashi, J.; Kawakami, K.; Kobayashi, Y.; Tarui, T. The First Direct Observation of Hydrogen Trapping Sites in TiC Precipitation-Hardening Steel through Atom Probe Tomography. *Scr. Mater.* **2010**, 63 (3), 261–264. <https://doi.org/10/fkrqw3>.
- (21) Srikant, V.; Clarke, D. R. On the Optical Band Gap of Zinc Oxide. *J. Appl. Phys.* **1998**, 83 (10), 5447–5451. <https://doi.org/10/bksxzf>.
- (22) van Dijken, A.; Meulenkaamp, E. A.; Vanmaekelbergh, D.; Meijerink, A. Identification of the Transition Responsible for the Visible Emission in ZnO Using Quantum Size Effects. *J. Lumin.* **2000**, 90 (3), 123–128. <https://doi.org/10/dfqqr>.
- (23) Janotti, A.; Van de Walle, C. G. Native Point Defects in ZnO. *Phys. Rev. B* **2007**, 76 (16), 165202. <https://doi.org/10.1103/PhysRevB.76.165202>.
- (24) Sombrio, C. I. L.; Franzen, P. L.; dos Reis, R.; Boudinov, H. I.; Baptista, D. L. Passivation of Defects in ZnO Nanowires by SiO₂ Sputtering Deposition. *Mater. Lett.* **2014**, 134, 126–129. <https://doi.org/10.1016/j.matlet.2014.07.066>.

- (25) R_{00} values for some Alexa Fluor dyes—Table 1.6 - US
<https://www.thermofisher.com/us/en/home/references/molecular-probes-the-handbook/tables/r0-values-for-some-alexa-fluor-dyes.html> (accessed May 20, 2019).
- (26) Efros, Al. L.; Rosen, M.; Kuno, M.; Nirmal, M.; Norris, D. J.; Bawendi, M. Band-Edge Exciton in Quantum Dots of Semiconductors with a Degenerate Valence Band: Dark and Bright Exciton States. *Phys. Rev. B* **1996**, *54* (7), 4843–4856.
<https://doi.org/10.1103/PhysRevB.54.4843>.
- (27) Nirmal, M.; Norris, D. J.; Kuno, M.; Bawendi, M. G.; Efros, Al. L.; Rosen, M. Observation of the “Dark Exciton” in CdSe Quantum Dots. *Phys. Rev. Lett.* **1995**, *75* (20), 3728–3731. <https://doi.org/10.1103/PhysRevLett.75.3728>.

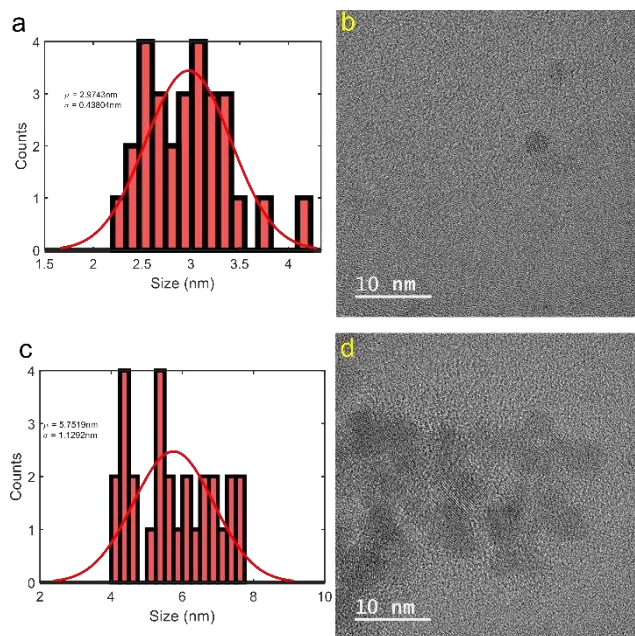
APPENDIX



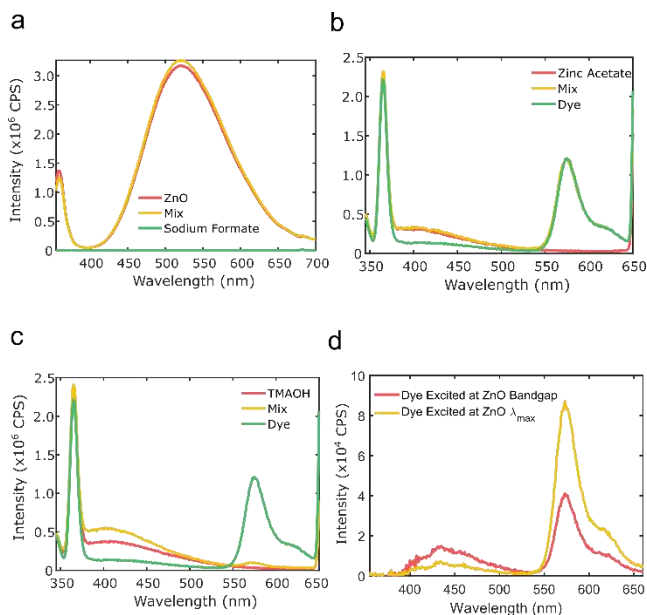
SI Figure 1. Effect of sonication on aggregation of ZnO. UV-Vis absorption spectra of unsonicated (red trace) and sonicated (yellow trace) ZnO. Sonication breaks up particle aggregates, decreasing the broad tail in the near-IR region.



SI Figure 2. Optical properties of sample over time. Defect (red squares) and bandgap (yellow circles) emission as a function of time.

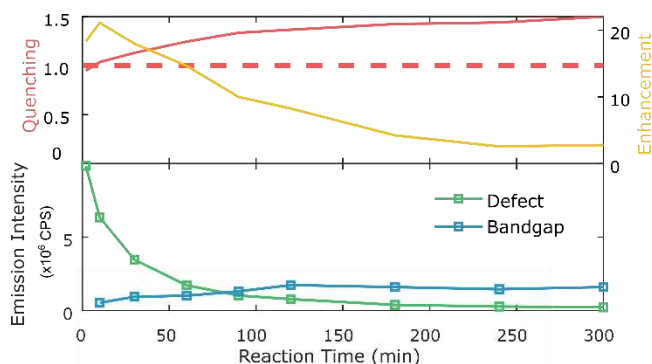


SI Figure 3. Particle size characterization. (a) Histogram of measured particle sizes from TEM analysis for 2 min ZnO. (b) Representative TEM image of 2 min ZnO. (c) Histogram of measured particle sizes from TEM analysis for 300 min ZnO. (d) Representative TEM image of 300 min ZnO.

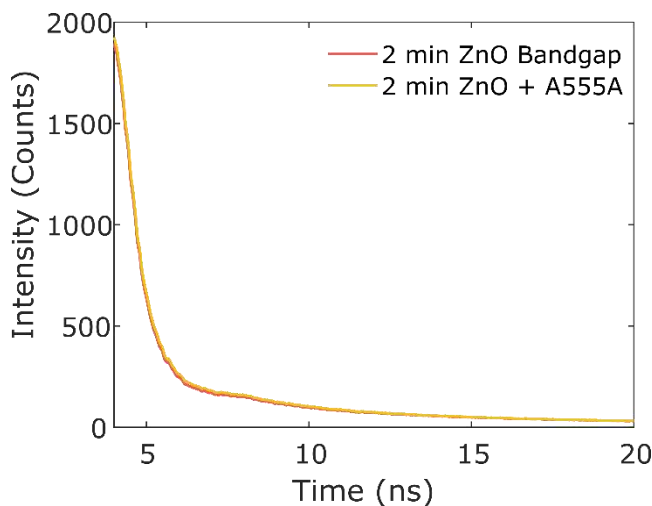


SI Figure 4. Control experiments. (a) Control experiment of ZnO (red trace) before and after the addition of a 100 nM sodium formate solution (formate alone green trace, mixture yellow trace). (b) Control experiment of A555 (green trace) before and after the addition of a 45 uM zinc acetate solution (zinc acetate alone red trace, mixture yellow trace). (c) Control experiment

of A555 (green trace) before and after the addition of a 45 μM TMAOH solution (TMAOH alone red trace, mixture yellow trace). **(d)** A555 excited at ZnO bandgap wavelength (red trace) and ZnO defect wavelength (yellow trace).



SI Figure 5. Energy transfer with 0.1 OD ZnO.



SI Figure 6. trPL of ZnO bandgap. ZnO was excited at 270 nm in the absence (red trace) and presence of A555 (yellow trace) and monitored at the bandgap emission (345 nm). No changes in lifetime were detected.

SI Table 1. Kinetic fit parameters.

Synthesis Time (min)	k_0 (ns^{-1})	k_{qt} (ns^{-1})	k_q (ns^{-1})	λ_t	λ_s	ϕ
2	0.0063	0.0251	0.1622	1.4706	0.1356	0.8378
30	0.0074	0.0269	0.1258	1.2205	0.2286	0.7857
180	0.0089	0.0342	0.0403	1.1008	0.9988	0.4832